Mathematical Biosciences and Engineering

http://www.aimspress.com/journal/MBE

MBE, 17(6): 7411–7427.
DOI: 10.3934/mbe.2020379
Received: 31 August 2020
Accepted: 21 October 2020
Published: 28 October 2020

Research article

Multi-objective optimization of peel and shear strengths in ultrasonic metal welding using machine learning-based response surface methodology

Yuquan Meng, Manjunath Rajagopal, Gowtham Kuntumalla, Ricardo Toro, Hanyang Zhao, Ho Chan Chang, Sreenath Sundar, Srinivasa Salapaka, Nenad Miljkovic, Placid Ferreira, Sanjiv Sinha, Chenhui Shao*

Department of Mechanical Science and Engineering, University of Illinois at Urbana-Champaign, Urbana, IL, USA

* **Correspondence:** Email: chshao@illinois.edu; Tel: +1-217-300-4750.

Abstract: Ultrasonic metal welding (UMW) is a solid-state joining technique with varied industrial applications. Despite of its numerous advantages, UMW has a relative narrow operating window and is sensitive to variations in process conditions. As such, it is imperative to quantitatively characterize the influence of welding parameters on the resulting joint quality. The quantification model can be subsequently used to optimize the parameters. Conventional response surface methodology (RSM) usually employs linear or polynomial models, which may not be able to capture the intricate, nonlinear input-output relationships in UMW. Furthermore, some UMW applications call for simultaneous optimization of multiple quality indices such as peel strength, shear strength, electrical conductivity, and thermal conductivity. To address these challenges, this paper develops a machine learning (ML)-based RSM to model the input-output relationships in UMW and jointly optimize two quality indices, namely, peel and shear strengths. The performance of various ML methods including spline regression, Gaussian process regression (GPR), support vector regression (SVR), and conventional polynomial regression models with different orders is compared. A case study using experimental data shows that GPR with radial basis function (RBF) kernel and SVR with RBF kernel achieve the best prediction accuracy. The obtained response surface models are then used to optimize a compound joint strength indicator that is defined as the average of normalized shear and peel strengths. In addition, the case study reveals different patterns in the response surfaces of shear and peel strengths, which has not been systematically studied in the literature. While developed for the UMW application, the method can be extended to other manufacturing processes.

Keywords: ultrasonic metal welding; mechanical strength; response surface methodology; process optimization; machine learning

1. Introduction

UMW is a solid-state joining method with various industrial applications including lithium-ion battery assembly [1–3], automotive body construction [4–6], and electronic packaging [7–9]. Among the advantages of UMW over conventional fusion welding techniques are the ability to join dissimilar metals, reduced energy consumption, and short welding cycles [1, 2, 10]. In addition, UMW is more environmentally friendly and free of solidification defects. It is thus considered as a promising joining technology contributing to the emerging trends in advanced manufacturing including electrification and lightweighting. It is documented that UMW can accommodate junctions of various combinations, including metal/metal, polymer/polymer, and metal/polymer [11, 12]. A typical UMW system is comprised of generator, transducer, booster, horn, and anvil, as shown by Figure 1. These components convert high-frequency voltage to high-frequency mechanical vibration, which subsequently joins workpieces together.

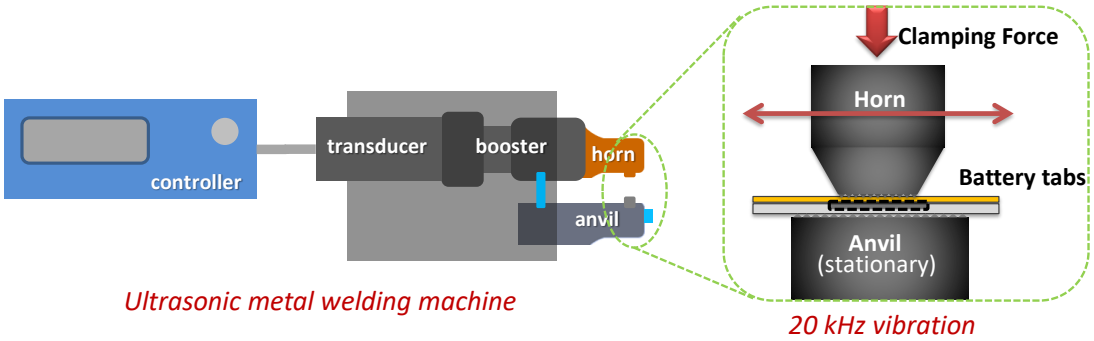

Figure 1. Schematic of a UMW system.

Despite of its numerous advantages, UMW has a relative narrow operating window and is sensitive to variations in process conditions. As such, quality control of UMW has received extensive attention, especially in industrial applications. Existing research on predicting UMW quality usually employs two types of approaches, namely, finite element simulations (e.g., [13, 14]) and data-driven online process monitoring (e.g., [15–18]). Xi et al. [13] developed finite element models to predict the mechanical performance of UMW joints under lap shear tests based on measured effective thickness and bonding length, which are obtained from microscopic analysis. Shen et al. [14] utilized finite element methods to predict the temperature profile and microstructure evolution during ultrasonic welding. Nonetheless, the finite element models are inherently computationally expensive, prohibiting cost-effective process optimization in practice and they fail to establish an end-to-end connection between input parameters and the output quality. Online process monitoring methods use in-situ sensing signals, e.g., power, vibration displacement, and audible signals, to infer on the joint quality. Key steps in the development of these methods include [17] (i) sensor selection, (ii) signal preprocessing, (iii) feature extraction, (iv) feature selection, e.g., [15], and (iv) quality prediction using artificial intelligence approaches, e.g., [16]. However, such methods assume that process parameters have been optimized offline and cannot account for the impact of process parameters on output quality.

The joint quality of UMW is influenced by a set of welding parameters including welding amplitude, welding time, clamping pressure, and welding pressure. Identifying the best combination of parameters, namely, process optimization, is still an open yet challenging question. In some industries,

trial and error approaches are still commonly used. Such methods require a large number of welding experiments, which is costly, time-consuming, and less accurate. Furthermore, it has been established that UMW has strong process variability due to uncontrollable process conditions such as surface contamination [3,19] and tool wear [17,20–24]. Although the adverse effects of such conditions have been qualitatively characterized in the literature, the direct link between these factors and joint quality is still missing. Therefore, a more effective and efficient approach for response surface modeling and process optimization is critically needed.

RSM is a data-driven methodology that explores the relationships between process inputs and one or multiple process outputs [25]. Statistical models such as linear and polynomial models are commonly used in RSM to characterize the input-output relationships based on experimental data obtained from a sequence of designed experiments. RSM is particularly useful when there is a lack of understanding on the physical process. In manufacturing, RSM has been successfully applied to different processes including machining [26, 27], friction spot welding [28], arc welding [29], resistance spot welding [30], and UMW [1]. A third-order polynomial function (or cubic function) was developed in [1] to characterize the influence of welding pressure and welding time on the resulting peel strength. The process complexity in UMW may lead to strong nonlinearities in the input-output relationships that cannot be adequately characterized by polynomial models. This motivates the application of ML models for response surface modeling due to their superior modeling capabilities. Some recent studies have explored using ML models for other manufacturing processes. For instance, an RBF was used to model the relationships between process parameters and performance responses in an electrical discharge machining process [31]. Yet, no studies exist on ML-based RSM for UMW.

The joint quality of UMW is often characterized by mechanical strength, which is commonly evaluated by peel and shear tests. While both testing methods are widely used in existing studies, the differences in the response surfaces of peel and shear strengths are not well understood. Furthermore, some applications call for the optimization of quality indices in addition to joint strength, such as electrical conductivity in electric vehicle batteries [2] and thermal conductivity in heat exchangers [32]. Consequently, a multi-objective optimization approach is highly desirable.

In this paper, we employ different ML models including spline regression, GPR, and SVR to characterize the influence of two welding parameters, namely, welding time and welding pressure, on the shear and peel strengths. Different kernels are used in GPR and SVR. We also compare the modeling performance of ML methods and polynomial models with first, second, and third orders based on a cross-validation procedure. Afterwards, the differences in response surfaces for shear and peel strengths are analyzed and discussed. Finally, the shear and peel strengths are jointly optimized using the best-performing response surface models.

This remainder of this paper is organized as follows. In Section 2, we introduce the response surface modeling methods used in this research. Section 3 presents the details of the experimental design and mechanical testing procedure. The main results are presented and discussed in Section 4. Section 5 concludes the paper and discusses possible future research.

2. ML-based response surface methodology

In this section, we present a brief introduction to polynomial regression and ML models used, including spline regression, GPR, and SVR.

2.1. Polynomial regression

One important goal of RSM is to construct a function $f(x)$ that can estimate the input-output relation of a process. Polynomial regression has been popularly used in conventional RSM. Suppose $x_1, x_2, ..., x_n$ is the training input, and $y_1, y_2, ..., y_n$ is the corresponding output. n is the number of training samples. The parameters in a polynomial model can be obtained by minimizing the prediction error, which is given by the Eq. (2.1).

$$L = \sum_{i=1}^{n}(y_i - \hat{y}_i)^2 = \sum_{i=1}^{n}(y_i - P(x_i))^2, \tag{2.1}$$

where $P(x)$ is the polynomial function to be found [33].

Polynomial functions with lower orders may not be able to express the complex response surfaces. On the other hand, a higher-order model generally has better modeling capability, but it may suffer from an overfitting issue. The choice of orders can be made based on the practitioner's experience or using a more rigorous model selection method. Furthermore, polynomial regression can capture the global tendency of the whole training dataset but may lose some delicate local topography.

2.2. Spline regression

Spline regression utilizes piecewise polynomial functions, called spline functions, to describe a complex relationship or function. Spline regression has a certain order of smoothness, i.e., a spline function f, defined on $[x_0, x_k]$, that satisfies:

$$f(x) = \begin{cases} P_0(x), x_0 \le x < x_1 \\ P_1(x), x_1 \le x < x_2 \\ \quad ... \\ P_{k-1}(x), x_{k-1} \le x \le x_k \end{cases} \tag{2.2}$$

and

$$f^{(p)}(x) \in \mathbf{C}(x_0, x_k), p = 1, 2, ...m - 1, \tag{2.3}$$

where $P_0(x), P_1(x), ..., P_{k-1}(x)$ are polynomials of order m. Cubic functions, i.e., $m = 3$, is a common choice. The points $x_0, x_1, ..., x_k$ are called knots. In multiple input variable problems, the spline function is constructed as the tensor product of each piecewise polynomial $P_i(\mathbf{x})$.

Spline regression models are capable of capturing the localized variations while ensuring high-level smoothness. In our case, there are two input variables. Hence the 2D spline function is employed. We use tensor product of each piecewise polynomial $P_i(x)$, displayed by Eq. (2.4). In this paper, the piecewise cubic function and the tensor product are used for 2D spline to construct the 2D spline function [34].

$$f(x, y) = P_i(x)P_j(y), x_i \le x < x_{i+1}, y_j \le y < y_{j+1}. \tag{2.4}$$

2.3. GPR

A Gaussian process is a collection of random variables such that the joint distribution of every finite subset of random variables is multivariate Gaussian. It can be considered as a Gaussian distribution

over functions, i.e.,

$$f(x) \sim GP(\mu(x), K(x, x') + \delta_{ij}\sigma^2), \tag{2.5}$$

where $m(x)$ and $K(x, x')$ are the mean and covariance functions. δ_{ij} is the Kronecker delta function. σ^2 is the variance of the noise. The prediction of GP is made by modeling the joint distribution based on training dataset, also called observations. Specifically, the collection of training points and test points are jointly multivariate Gaussian distributed [35]:

$$\begin{bmatrix} f \\ f^* \end{bmatrix} \sim N\left(\begin{bmatrix} \mu \\ \mu^* \end{bmatrix}, \begin{bmatrix} K(X,X) + \sigma^2 I & K(X,X^*) \\ K(X^*,X) & K(X^*,X^*) \end{bmatrix}\right). \tag{2.6}$$

Then the prediction is given by:

$$f^*|X, y, X^* \sim N(\bar{f}^*, \Sigma^*), \tag{2.7}$$

$$\bar{f}^* = \mu^* + K(X^*, X)[K(X,X) + \sigma^2 I]^{-1}(y - \mu), \tag{2.8}$$

$$\Sigma^* = K(X^*, X^*) + K(X^*, X)[K(X,X) + \sigma^2 I]^{-1}K(X, X^*). \tag{2.9}$$

The performance of GPR is largely determined by the kernel function. Common choices for kernel functions include RBF and rational quadratic (RQ) function, which are shown by Eq. (2.10) and Eq. (2.11), respectively. In this paper, RBF and RQ kernels are used.

$$K(x, y) = \exp\left(-\frac{\|x - y\|^2}{2\sigma_0^2}\right). \tag{2.10}$$

$$K(x, y) = \left(1 + \|x - y\|^2\right)^{-\alpha}. \tag{2.11}$$

2.4. SVR

The basic idea of SVR is to find a function $f(x)$ that can estimate the targets y_i given training data x_i and has at most ϵ deviation while ensuring the flatness of $f(x)$ [36]. The simplest form for $f(x)$ is the linear function, i.e.,

$$f(x) =< w, x > +b, \tag{2.12}$$

where w is the weight, b represents bias, and $< \cdot, \cdot >$ refers to the inner product. Then the problem can be written as

$$\begin{gathered} \min \ \frac{1}{2}\|w\|^2 + C\sum_i^n \xi_i, \\ \text{subject to } \|y_i - < w, x_i > -b\| \le \epsilon + \xi_i, \\ \xi_i \ge 0, \end{gathered} \tag{2.13}$$

where C is the trade-off between flatness of f and the deviation.

Similar to GPR, the concept of kernels is introduced in SVR to solve nonlinear problems. The most commonly adopted kernels are:

- polynomial kernel:

$$K(x, y) = (< x, y > +1)^d. \tag{2.14}$$

- RBF kernel:

$$K(x, y) = \exp\left(-\frac{\|x - y\|^2}{2\sigma_0^2}\right). \tag{2.15}$$

By solving the Lagrangian dual [36], the SVR for nonlinear problem can be described in the following optimization problem:

$$\begin{gathered}\min -\frac{1}{2}\sum_{i,j=1}^{n}(\alpha_i - \alpha_i^*)(\alpha_j - \alpha_j^*)K(x_i, x_j) - \epsilon\sum_{i=1}^{n}(\alpha_i + \alpha_i^*) + \sum_{i=1}^{n} y_i(\alpha_i - \alpha_i^*) \\ \text{subject to } \sum_{i=1}^{n}(\alpha_i - \alpha_i^*) = 0 \text{ and } \alpha_i, \alpha_i^* \in [0, C].\end{gathered} \tag{2.16}$$

and f has the form of

$$f(x) = \sum_{i=1}^{n}(\alpha_i - \alpha_i^*)K(x, x_i) + b. \tag{2.17}$$

3. Joining configurations and mechanical testing

3.1. Experimental setup

110-copper sheet with the thickness of 0.254 mm is used for the welding experiments. The copper sheet is trimmed into small pieces in the dimension of 76 mm × 51 mm. Before welding, cleaning wipes are used to remove the pollutants on the copper specimen. The Branson Ultraweld L20 Spot Welder, shown in Fig 1(b), is employed to perform UMW experiment. Time mode is selected in this experiment.

In UMW, welding amplitude, welding time, clamping pressure, and welding pressure are dominant factors influencing the joint strength. Welding amplitude refers to the amplitude of the horn's cyclic movement. It does not only directly affects the material softening process but also influences the rate of frictional heat generation. Welding time determines the duration of a welding process. It can change the final joint quality through influencing the amount of frictional heat generated. Clamping pressure (or trigger pressure) refers to the pre-load pressure that triggers ultrasonics. Welding pressure refers to the pressure applied vertically to the workpieces during the welding process. In this study, welding amplitude, ranging from 40 μm to 55 μm, and welding time, ranging from 0.40 s to 0.80 s, are selected to be the process/independent variables (inputs), whereas clamping and welding pressure are fixed at 50 psi. The parameters and number of repeats for each testing configuration are shown in Table 1.

3.2. Mechanical testing

Two types of mechanical testing, i.e., peel and shear testing, are applied to measure the joint strength. Figure 2(a) and (b) shows the configurations of shear and peel tests, respectively. In a shear

Table 1. Welding configurations and replicates

Welding Time (s)	Welding Amplitude (μm)	Number of Repeats-Shear	Number of Repeats-Peel
0.40	40	10	4
0.45	40	10	4
0.50	40	11	4
0.55	40	10	4
0.60	40	10	4
0.65	40	5	4
0.70	40	5	4
0.75	40	5	4
0.80	40	5	4
0.40	45	10	4
0.45	45	10	4
0.50	45	10	4
0.55	45	9	4
0.60	45	10	4
0.65	45	5	4
0.70	45	5	4
0.75	45	5	4
0.80	45	5	4
0.40	50	9	4
0.45	50	10	4
0.50	50	13	4
0.55	50	9	4
0.60	50	10	4
0.65	50	5	4
0.70	50	5	4
0.75	50	5	4
0.80	50	5	4
0.40	55	10	4
0.45	55	10	4
0.50	55	10	4
0.55	55	10	4
0.60	55	10	4
0.70	55	5	4
0.80	55	5	4

test, the load is prescribed parallel to the bonding surface. Whereas in peel test, the load is applied perpendicular to the joint surface. In both tests, the instantaneous load is recorded until the two layers are completely separated. Figure 2(c) shows a photo of the Instron universal testing machine used for peel and shear testing. The configuration of the testing machine and data sampling frequency is shown in Table 2.

Table 2. Testing protocol followed in our experiments

Test type	Ramp slope (mm/s)	Sampling frequency (ms)	Joint dimensions
Peel	1	10	8 mm diameter
Shear	0.3	10	8 mm diameter

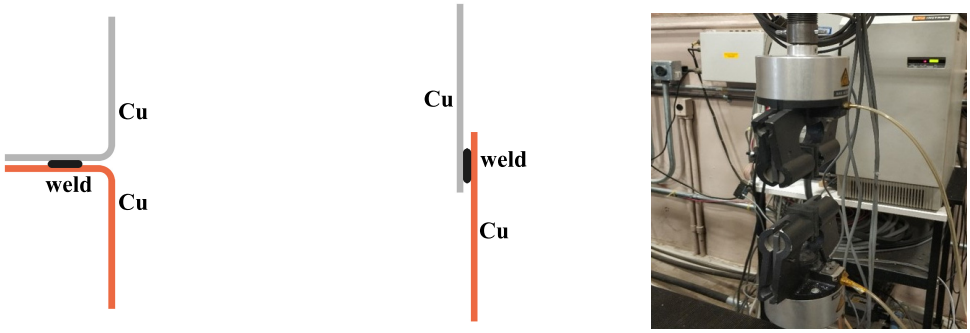

(a) Specimen configuration for peel test

(b) Specimen configuration for shear test

(c) The Instron universal testing machine used in this study

Figure 2. The configurations of peel and shear tests.

4. Results and discussion

In this section, results from the mechanical testing, including peel test and shear test, are presented, where different failure modes are identified. Moreover, different ML models are used to obtain the response surfaces, and their performance is compared with polynomial regression. Finally, the response surface models are used to identify the optimal parameters for a compound joint strength indicator.

4.1. Mechanical strength

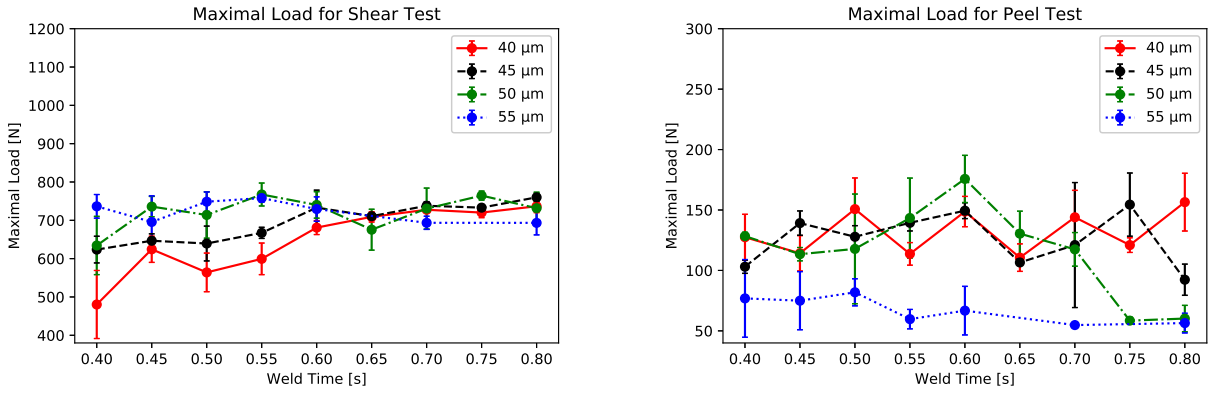

(a) Shear strength

(b) Peel strength

Figure 3. Mechanical strengths vs. welding time under different welding amplitudes.

We observe three different failure modes in both peel and shear tests, which are closely related to the weld types. The formation of those failure modes can be ascribed to the reduction of base material strength and enhancement of joint strength. Due to the plastic deformation and longitudinal cyclic motion of horn during welding, the base material is removed from the weld zone and flows to the peripheral area. Such material loss rises as the welding progresses, resulting in a decrease in base

material strength, meanwhile the ultrasonic bonding strength increases. Depending on the relative strengths of base materials and joints, the weld types can be categorized in three types.

- *Cold weld:* The joint is not fully developed but the material base is hardly removed. In mechanical testing, only the joint is separated.
- *Good weld:* The strength of joint and the base material are close or at the same level. In mechanical testing, partial of joint and base materials are torn down.
- *Over weld:* The base material at junction is weaker than the joint. In mechanical testing, only base material adjacent to weld region is separated.

It should be noted that it is possible that an over weld in shear test can also be good or cold weld in peel test, since the relative strength of base material to joint may vary in different loading types.

In this study, we select the maximum load as the joint strength in both shear and peel tests. Other indicators such as energy absorbed during mechanical testing may also be used [13]. The outliers, due to wrong welding configuration or inappropriate clamping position in mechanical testing, are removed using a 1-sigma criterion. Figure 3 shows the relationship between shear/peel strengths and welding time under different welding amplitude values.

The shear test result is shown in Figure 3(a). For both 40 μm and 45 μm, the shear strength increases as the welding time increases, while the slope of 40 μm is larger than that of 45 μm. The increasing trend indicates that the joint forms progressively as the weld continues and the welding time increases. Additionally, 45 μm has a larger strength than 40 μm, but they converge to the same level when welding time reaches 0.65 s. On the other hand, the overall trends for 50 μm and 55 μm are similar, except that for 55 μm there is a drop in shear strength when welding time increases over 0.65. This indicates an increased likelihood for over welds.

Table 3. Training and testing RMSEs of different methods. The last column refers to the sum of prediction errors for shear and peel strengths. The models with best performance in each category are highlighted in bold.

	Shear Strength RMSE [N]		Peel Strength RMSE [N]		Total Testing
	Training	Testing	Training	Testing	RMSE
Spline	22±1	52±43	12±1	35±16	85
GPR-RBF	29± 1	26±14	20± 8	**24**± 11	**50**
GPR-RQ	**7**± 1	32± 11	**2** ± 2	26± 12	58
SVR-RBF	30± 1	**25**± 13	20± 1	25± 15	**50**
SVR-quad	30± 1	30± 9	21± 1	25± 13	55
Linear	53±1	37±13	41±1	34±15	73
Quadratic	27±1	27±11	20±1	**24**±14	51
Cubic	26±1	28±12	19±1	26 ±15	54

It is observed from Figure 3(b) that when the welding amplitude is low, the weld strength maintains at a relatively high value. The trend for welding amplitude of 40 μm is the most stable. This is because the amplitude of 40 μm is lower than the threshold to form a good weld. Even by increasing the welding time, the central temperature and plastic deformation of weld region do not dramatically rise, hence almost no improvement in strength is observed. The trends for welding amplitudes of 40 μm and 45 μm both have a critical point, after which a significant drop in peel strength occurs, indicating

the occurrence of over welds. The critical points are 0.75 s and 0.80 s for 45 μm and for 50 μm, respectively. When the welding amplitude reaches 55 μm, the weld strength is very low regardless of welding time. This is attributed to the fact that all welds are over welds, which lead to much lower strength.

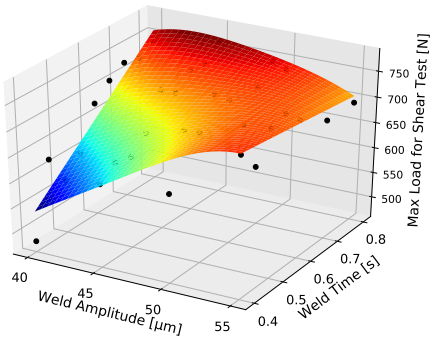

(a) Response surface for the shear strength

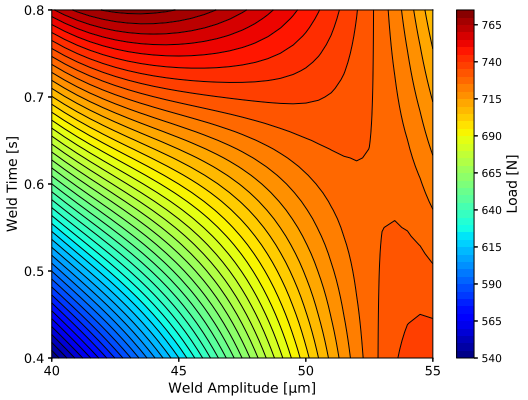

(b) Contour of the shear strength

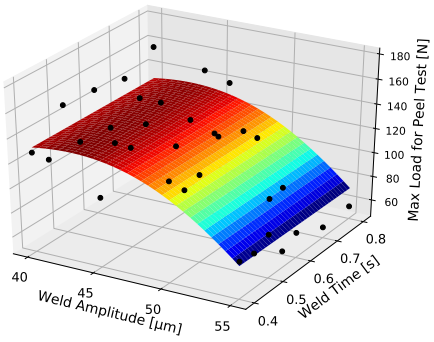

(c) Response surface for the peel strength

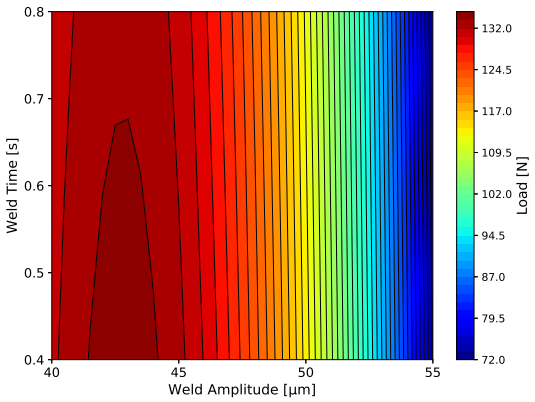

(d) Contour of the peel strength

Figure 4. Response surfaces obtained by GPR-RBF.

4.2. Joint strength prediction

To illustrate the performance of different models, the obtained response surfaces are evaluated on the dataset using leave-two-out cross-validation, which is selected because of the small dataset we have. In each round of cross-validation, the full dataset is randomly partitioned into a training and a test set, which include 32 and 2 configurations, respectively. Root-mean-square error (RMSE) is selected as the modeling performance indicator, because it is smoothly differentiable and minimizing such metric gives exactly the mean value [37]. RMSEs are averaged over all rounds to evaluate the prediction performance.

Table 3 shows the prediction accuracy of spline regression, GPR with RBF and RQ kernels, SVR

with RBF and quadratic kernels, and polynomial regression with different orders. SVR-RBF has the smallest testing error on shear strength, while SVR-quad and the quadratic function perform the best accuracy on peel strength. SVR-quad has smaller prediction uncertainty than the quadratic function. Though spline regression and SVR-RQ have small training errors for both shear and peel strengths, their testing errors are much larger, indicating an overfitting issue.

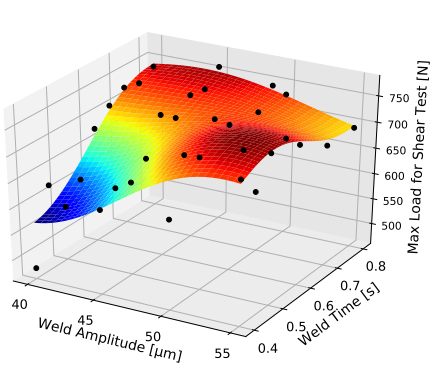

(a) Response surface for the shear strength

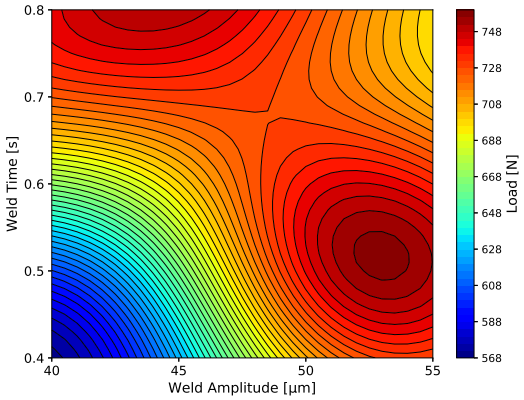

(b) Contour of the shear strength

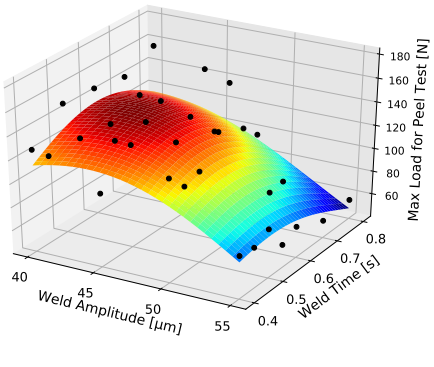

(c) Response surface for the peel strength

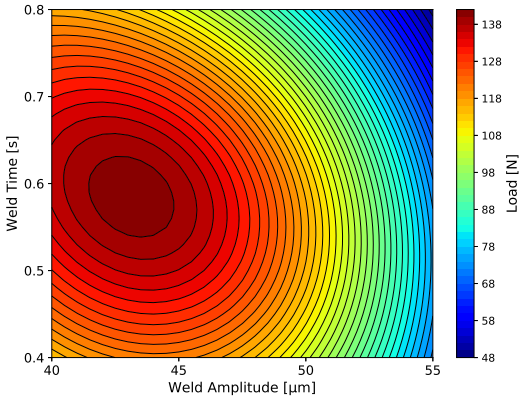

(d) Contour of the peel strength

Figure 5. Response surfaces obtained by SVR-RBF.

Figure 4, 5, and 6 illustrate the response surfaces obtained by GPR-RBF, SVR-RBF, and quadratic regression, respectively. The topography and optimal parameters indicated by response surfaces are different for different models. It is estimated that in GPR-RBF (Figure 4b) and quadratic regression (Figure 6b) the maximal shear strength occurs beyond the range of parameters selected in this study, whereas the maximum locates inside the parameter range in SVR-RBF (Figure 5b). In contrast, all the maxima of peel strength are inside the parameter range (Figure 4d, 5d and 6d). Interestingly, the response surfaces for shear and peel strengths are intrinsically different. The response surfaces for shear strength all have two local maxima and the strengths of two peaks are comparable, as depicted in Figure 4b, 5b, and 6b. Nevertheless, such phenomenon does not hold for the peel strength, for which

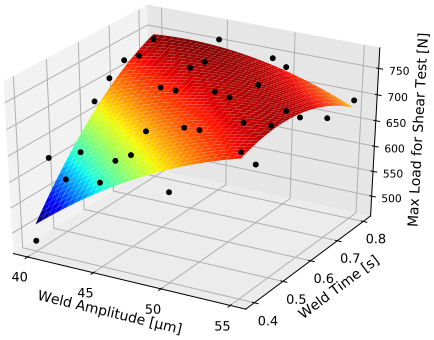

(a) Response surface for the shear strength

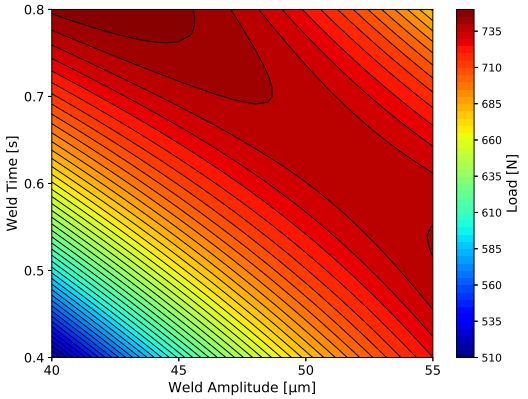

(b) Contour of the shear strength

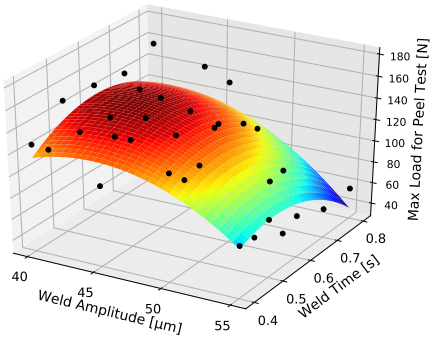

(c) Response surface for the peel strength

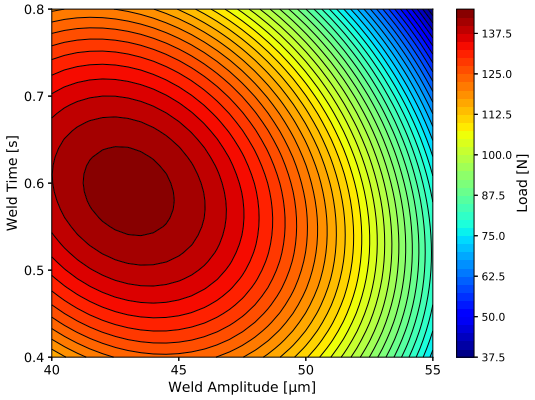

(d) Contour of the peel strength

Figure 6. Response surfaces obtained by quadratic regression.

there is only one peak (see Figure 4d, 5d, and 6d). The peel strength decreases sharply when moving away from the global maximum. One possible explanation is that the damaged edges of over-weld joints in peel testing are easy to break due to the normal load exerted to the joint. Slight tearing of the joint surface will significantly deteriorate the joint strength. In contrast, the load in shear testing is applied in parallel with the joint surface, so the shear strength is less sensitive to the tearing of the joint surface.

To determine the optimal weld parameters for both shear and peel strengths, the criterion of normalized sum is adopted, i.e., the goal is to maximize a compound strength indicator:

$$F = \frac{1}{2}\left(\frac{F_{peel}(x,y)}{F_{peel,max}} + \frac{F_{shear}(x,y)}{F_{shear,max}}\right), \tag{4.1}$$

where F_{peel} and F_{shear} represent peel and shear strengths, respectively.

The contour plot for F is illustrated in Figure 7. The region in red color can be considered as good weld region. It is seen that the welding time needed to form a good weld decreases approximately linearly as the welding amplitude increases. When the welding amplitude exceeds the optimal value, the

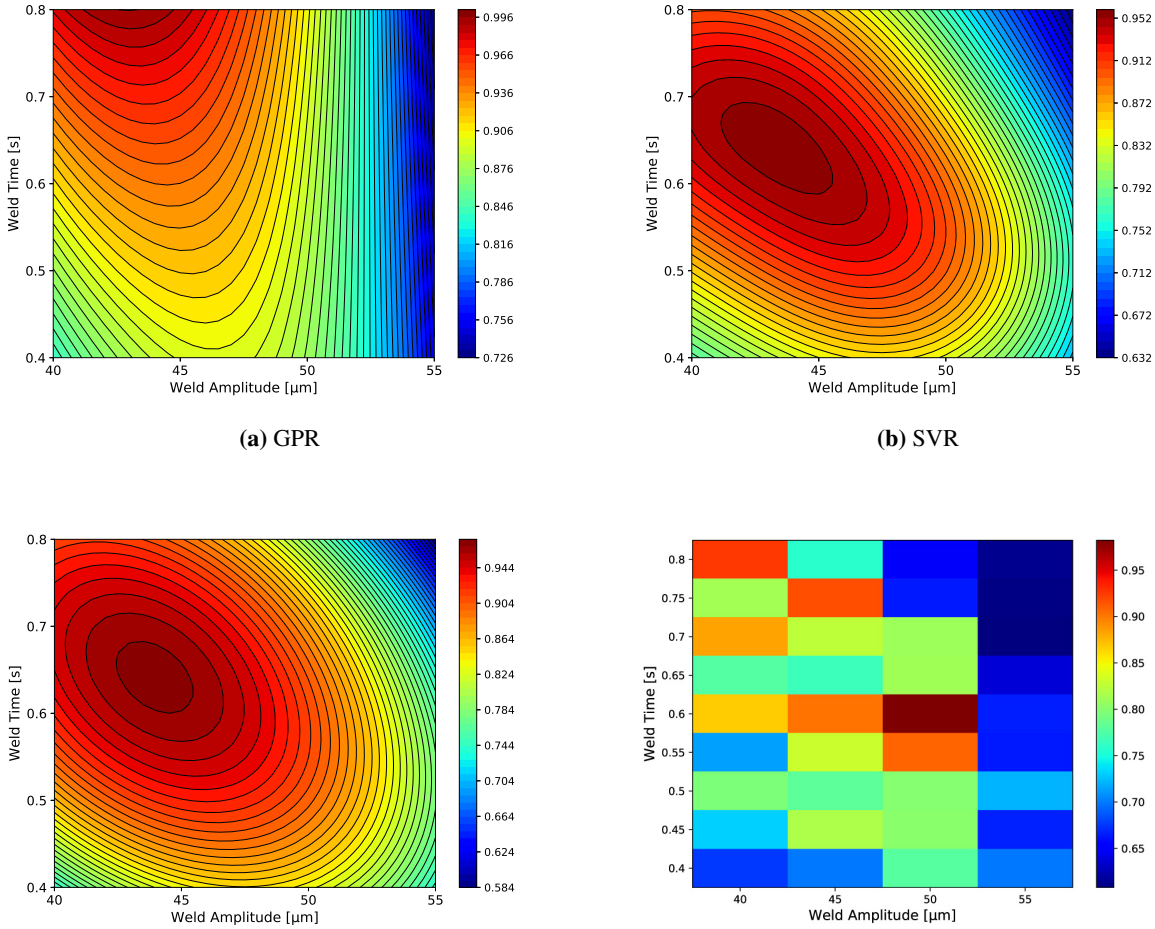

(a) GPR

(b) SVR

(c) Quadratic regression

(d) Ground truth

Figure 7. Contour plot of the sum of normalized maximal peel and shear load.

Table 4. Optimal parameters for the compound strength obtained by different methods.

	Optimal Parameters		
	Weld Amplitude	Weld Time	Optimal Value
GPR	43.0	0.80	0.996
SVR	43.5	0.64	0.975
Quadratic	44.0	0.64	0.972
Ground Truth	50.0	0.60	0.983

compound strength drops drastically no matter what the welding time is. This indicates the existence of a threshold for welding amplitude, after which the over weld dominates. GPR-RBF, SVR-RBF, and quadratic regression give different global maxima, as shown by Table 4. Figure 7d shows the ground truth of the compound strength calculated from the experiment results. Though being low resolution because of the limited number of experiments, Figure 7d shows a ringlike pattern, which agrees with Figure 7a-c, and the threshold for welding amplitude is also consistent with all regression models. Compared with the ground truth (50 μm, 0.60 s), the outcomes by SVR-RBF and quadratic regression are more accurate than that of GPR-RBF.

5. Conclusion

In this paper, we developed an ML-based RSM for two performance indicators in UMW—shear and peel strengths. The performance of spline regression, GPR, SVR, and polynomial regression was compared using a dataset collected from UMW experiments where the values of welding amplitude and welding time were varied. The trained response surface models were subsequently used to find the optimal parameters for a compound strength indicator, which was defined as the average of normalized shear and peel strengths. It was shown that ML methods hold good potential in modeling input-output relationships in UMW.

The experimental results indicate the existence of a threshold for the welding amplitude threshold at which point over welds start to occur and dominate afterwards. A clear trend of welding strength transition in the peel strength is observed at 50 μm, implying the weld quality undergoes the transition from cold weld to good weld, and to over weld.

A comparison between the response surfaces of shear and peel strengths leads to some interesting observations. First, the shear strength stays at a much higher level than the peel strength. Second, the response surface of the shear strength presents two peaks with comparable strength values, but the peel strength only has one global peak. Their distributions are also very different. The compound strength indicator reaches its peak at modest values of both welding amplitude and welding time.

Future research can be conducted in the following directions. First, more welding parameters such as clamping pressure and welding pressure will be introduced to create a larger dataset. It is expected when more parameters are included, machine learning methods may gain a larger advantage due to their advanced modeling capability. Second, process variability should be taken into account and appropriately modeled, because repeatable, reliable performance is of utmost importance to manufacturers. Finally, other quality indices such as thermal and electrical conductivity should be considered, leading to an increased number of objectives for optimization.

Acknowledgments

We acknowledge support from the Advanced Manufacturing office (AMO) of the office of Energy Efficiency and Renewable Energy (EERE) under the U.S. Department of Energy (DOE) through the contract DE-EE0008312 and the National Science Foundation under Grant No. 1944345.

Conflict of interest

The authors have no conflict of interest.

References

1. T. H. Kim, J. Yum, S. J. Hu, J. Spicer, J. A. Abell, Process robustness of single lap ultrasonic welding of thin, dissimilar materials, *CIRP Annals*, **60** (2001), 17–20.
2. W. Cai, *Ultrasonic welding of lithium-ion batteries*, ASME Press, 03, 2017.
3. L. Nong, C. Shao, T. H. Kim, S. J. Hu, Improving process robustness in ultrasonic metal welding of lithium-ion batteries, *J. Manuf. Syst.*, **48** (2018), 45–54.
4. A. Siddiq, E. Ghassemieh, Thermomechanical analyses of ultrasonic welding process using thermal and acoustic softening effects, *Mech. Mater.*, **40** (2008), 982–1000.
5. C. Zhang, D. Chen, A. Luo, Joining 5754 automotive aluminum alloy 2-mm-thick sheets using ultrasonic spot welding, *Weld. J.*, **93** (2014), 131–138.
6. Z. Ni, F. Ye, Ultrasonic spot welding of aluminum alloys: A review, *J. Manuf. Process*, **35** (2018), 580–594.
7. H. P. C. Daniels, Ultrasonic welding, *Ultrasonics*, **3** (1965), 190–196.
8. J. Kim, M. Chiao, L. Lin, Ultrasonic bonding of In/Au and Al/Al for hermetic sealing of MEMS packaging, in *Technical Digest. MEMS 2002 IEEE International Conference. Fifteenth IEEE International Conference on Micro Electro Mechanical Systems (Cat. No. 02CH37266)*, IEEE, (2002), 415–418.
9. J. Kim, B. Jeong, M. Chiao, L. Lin, Ultrasonic bonding for MEMS sealing and packaging, *IEEE T. Adv. Packag.*, **32** (2009), 461–467.
10. S. Kumar, C. Wu, G. Padhy, W. Ding, Application of ultrasonic vibrations in welding and metal processing: A status review, *J. Manuf. Process*, **26** (2017), 295–322, 2017.
11. S. Krüger, G. Wagner,D. Eifler, Ultrasonic welding of metal/composite joints, *Adv. Eng. Mater.*, **6** (2004), 157–159.
12. Y. Meng, D. Peng, Q. Nazir, G. Kuntumalla, M. C Rajagopal, H. C. Chang, et al., Ultrasonic welding of soft polymer and metal: a preliminary study, in *International Manufacturing Science and Engineering Conference*, American Society of Mechanical Engineers, **58752** (2019), V002T03A083.
13. L. Xi, M. Banu, S. J. Hu, W. Cai, J. A. Abell, Performance prediction for ultrasonically welded dissimilar materials joints, *J. Manuf. Sci. Eng.*, **139** (2017), 011008.
14. N. Shen, A. Samanta, H. Ding, W. Cai, Simulating microstructure evolution of battery tabs during ultrasonic welding, *J. Manuf. Process*, **23** (2016), 306–314.
15. C. Shao, K. Paynabar, T. H. Kim, J. J. Jin, S. J. Hu, J. P. Spicer, et al., Feature selection for manufacturing process monitoring using cross-validation, *J. Manuf. Syst.*, **32** (2013), 550–555.

16. W. Guo, C. Shao, T. H. Kim, S. J. Hu, J. Jin, J. P. Spicer, et al., Online process monitoring with near-zero misdetection for ultrasonic welding of lithium-ion batteries: An integration of univariate and multivariate methods, *J. Manuf. Syst.*, **38** (2016), 141–150.

17. C. Shao, T. H. Kim, S. J. Hu, J. A. Abell, J. P. Spicer, et al., Tool wear monitoring for ultrasonic metal welding of lithium-ion batteries, *J. Manuf. Sci. Eng.*, **138** (2016), 051005.

18. Z. Ma, Y. Zhang, Characterization of multilayer ultrasonic welding based on the online monitoring of sonotrode displacement, *J. Manuf. Process.*, **54** (2020), 138–147.

19. S. S. Lee, C. Shao, T. H. Kim, S. J. Hu, E. K. Asibu, W. Cai, et al., Characterization of ultrasonic metal welding by correlating online sensor signals with weld attributes, *J. Manuf. Sci. Eng.*, **136** (2014), 051019.

20. C. Shao, W. Guo, T. H. Kim, J. J. Jin, S. J. Hu, J. P. Spicer, et al., Characterization and monitoring of tool wear in ultrasonic metal welding, In *9th International Workshop on Microfactories*, (2014), 161–169.

21. Y. Zerehsaz, C. Shao, and J. Jin, Tool wear monitoring in ultrasonic welding using high-order decomposition, *J. Intell. Manuf.*, **30** (2019), 657–669.

22. C. Shao, J. Jin, S. J. Hu, Dynamic sampling design for characterizing spatiotemporal processes in manufacturing, *J. Manuf. Sci. Eng.*, **139** (2017), 101002.

23. Y. Yang, C. Shao, Spatial interpolation for periodic surfaces in manufacturing using a Bessel additive variogram model, *J. Manuf. Sci. Eng.*, **140** (2018), 061001.

24. Y. Yang, Y. Zhang, Y. D. Cai, Q. Lu, S. Koric, C. Shao, Hierarchical measurement strategy for cost-effective interpolation of spatiotemporal data in manufacturing, *J. Manuf. Syst.*, **53** (2019), 159–168.

25. R. H. Myers, D. C. Montgomery, C. M. Anderson-Cook, *Response surface methodology: process and product optimization using designed experiments*, John Wiley & Sons, 2016.

26. H. K. Kansal, S. Singh, P. Kumar, Parametric optimization of powder mixed electrical discharge machining by response surface methodology, *J. Mater. Process Tech.*, **169** (2005), 427–436.

27. K. H. Hashmi, G. Zakria, M. B. Raza, S. Khalil, Optimization of process parameters for high speed machining of ti-6al-4v using response surface methodology, *Int. J. Adv. Manuf. Tech.*, **85** (2016), 1847–1856.

28. A. H. Plaine, A. R. Gonzalez, U. F. H. Suhuddin, J. F. Dos Santos, N. G. Alcântara, Process parameter optimization in friction spot welding of AA5754 and Ti6Al4V dissimilar joints using response surface methodology, *Int. J. Adv. Manuf. Tech.*, **85** (2016), 1575–1583.

29. S. Srivastava, R.K. Garg, Process parameter optimization of gas metal arc welding on is: 2062 mild steel using response surface methodology, *J. Manuf. Process.*, **25** (2017), 296–305.

30. D. Zhao, Y. Wang, S. Sheng, Z. Lin, Multi-objective optimal design of small scale resistance spot welding process with principal component analysis and response surface methodology, *J. Intell. Manuf.*, **25** (2014), 1335–1348.

31. X. Li, F. Yan, J. Ma, Z. Chen, X. Wen, Y. Cao, RBF and NSGA-II based EDM process parameters optimization with multiple constraints, *Math. Biosci. Eng.*, **16** (2019), 5788–5803.

32. G. Kuntumalla, Y. Meng, M. Rajagopal, R. Toro, H. Zhao, H. C. Chang, et al., Joining techniques for novel metal polymer hybrid heat exchangers, In *ASME International Mechanical Engineering Congress and Exposition*, American Society of Mechanical Engineers, **59384** (2019), V02BT02A018.

33. G. James, D. Witten, T. Hastie, R. Tibshirani, *An introduction to statistical learning*, Springer, 2013.

34. J. Friedman, T. Hastie, R. Tibshirani, *the elements of statistical learning*, Springer series in statistics, New York, 2001.

35. C. Rasmussen, C. Williams, *Gaussian process for machine learning*, the MIT Press, 2006.

36. A. J Smola, B. Schölkopf, A tutorial on support vector regression, in *Statistics and Computing*, **14** (2004), 199–222.

37. I. Goodfellow, Y. Bengio, A. Courville, *Deep Learning*, the MIT Press, 2016.

AIMS Press